LETTER

doi:10.1038/nature25446

Early episodes of high-pressure core formation preserved in plume mantle

Colin R. M. Jackson[1,2], Neil R. Bennett[1], Zhixue Du[1], Elizabeth Cottrell[2] & Yingwei Fei[1]

The decay of short-lived iodine (I) and plutonium (Pu) results in xenon (Xe) isotopic anomalies in the mantle that record Earth's earliest stages of formation[1–8]. Xe isotopic anomalies have been linked to degassing during accretion[2–4], but degassing alone cannot account for the co-occurrence of Xe and tungsten (W) isotopic heterogeneity in plume-derived basalts[9,10] and their long-term preservation in the mantle. Here we describe measurements of I partitioning between liquid Fe alloys and liquid silicates at high pressure and temperature and propose that Xe isotopic anomalies found in modern plume rocks (that is, rocks with elevated ^{3}He/^{4}He ratios) result from I/Pu fractionations during early, high-pressure episodes of core formation. Our measurements demonstrate that I becomes progressively more siderophile as pressure increases, so that portions of mantle that experienced high-pressure core formation will have large I/Pu depletions not related to volatility. These portions of mantle could be the source of Xe and W anomalies observed in modern plume-derived basalts[2–4,9,10]. Portions of mantle involved in early high-pressure core formation would also be rich in FeO[11,12], and hence denser than ambient mantle. This would aid the long-term preservation of these mantle portions, and potentially points to their modern manifestation within seismically slow, deep mantle reservoirs[13] with high ^{3}He/^{4}He ratios.

Mantle plumes contain components with high ^{3}He/^{4}He ratios that have been broadly interpreted as evidence for a primordial reservoir within Earth[1,14] (hereafter high-^{3}He/^{4}He mantle is referred to as 'plume mantle'). Recent high-precision analyses of Xe isotopes from plume mantle reveal a common signature of a low ^{129}Xe*/^{136}Xe*$_{Pu}$ ratio compared to mid-ocean-ridge basalt (MORB) mantle[2–4]. ^{129}Xe* is the decay product of short-lived and volatile ^{129}I. ^{136}Xe*$_{Pu}$ is the decay product of short-lived and refractory ^{244}Pu. Consequently, low ^{129}Xe*/^{136}Xe*$_{Pu}$ ratios for plume mantle have been interpreted to reflect an early depletion of I related to degassing of materials accreted to Earth[2,4].

Other observations of plume mantle, however, are not readily explained by degassing processes. Modern plume mantle contains W isotopic anomalies, both higher and lower than MORB mantle[9,10], that result from the decay of short-lived hafnium (^{182}Hf). In contrast to I, both W and Hf are refractory and not affected by degassing. W anomalies reflect the separation of core-forming metal from the silicate mantle early in Solar System history owing to the strong tendency of the core to incorporate W and fractionate Hf/W ratios within terrestrial bodies[15–18]. Moreover, early accretion of volatile-poor material, as would be required to generate low ^{129}Xe*/^{136}Xe*$_{Pu}$ ratios related to I volatility, would result in FeO-poor, buoyant mantle[11], which would be difficult to sequester and preserve at the base of the mantle where plumes originate[19]. In this study, we test the hypothesis that Xe and W anomalies in plume mantle were generated by the same process—core formation at high pressures—by quantifying how I partitions between liquid Fe alloy and liquid silicate at equilibrium ($D^{\mathrm{I}}_{\mathrm{met/sil}} = [\mathrm{I}]_{\mathrm{met}}/[\mathrm{I}]_{\mathrm{sil}}$, where brackets denote concentration).

Limited experimental data at 2–20 GPa (about 2,800 K) demonstrate that I can be siderophile and that its partitioning behaviour is affected by alloying components in liquid Fe[20], but the pressure, temperature and compositional (P–T–X) dependencies of $D^{\mathrm{I}}_{\mathrm{met/sil}}$ remain unknown under conditions directly relevant to deep magma oceans. If $D^{\mathrm{I}}_{\mathrm{met/sil}}$ values are sensitive to P–T–X under the conditions associated with core formation, then I/Pu variations should be formed with co-variations in Hf/W in the mantle. Over time, these co-variations of I/Pu and Hf/W would evolve coupled Xe and W anomalies if mixing with the remaining mantle was limited.

We define the P–T–X dependencies of $D^{\mathrm{I}}_{\mathrm{met/sil}}$ by conducting partitioning experiments in a laser-heated diamond anvil cell (DAC) (beamline 13-ID-D at the Advanced Photon Source) at temperatures from 3,100 K to 4,900 K, pressures from 20 GPa to 45 GPa, and oxygen fugacity from −0.5 to −2.0 logarithmic units relative to the iron–wüstite buffer (Methods, Supplementary Table 1). These are conditions directly relevant to deep magma oceans and related core formation events (such as in ref. 11). Cross-sections of heating spots were exposed for chemical analysis using a focused ion beam (Fig. 1).

The concentration of I and other elements in metal and silicate phases were quantified using a JEOL 8530F microprobe (Methods). Measured $D^{\mathrm{I}}_{\mathrm{met/sil}}$ values (as atomic ratios) vary from 0.32 to 14 ($n = 18$, Table 1). To relate $D^{\mathrm{I}}_{\mathrm{met/sil}}$ variations in the present experiments to P–T–X conditions of core formation, we conducted a stepwise, unweighted least-squares regression (Methods, Extended Data Fig. 1, Supplementary Table 2):

$$\ln(D^{\mathrm{I}}_{\mathrm{met/sil}}) = (461 \pm 147)P/T - (12 \pm 3)X^{\mathrm{S}}_{\mathrm{met}} - (21 \pm 4)X^{\mathrm{O}}_{\mathrm{met}} - (5 \pm 1) - \ln(\gamma^{\mathrm{Fe}}_{\mathrm{met}}) \quad (1)$$

where

$$X^{i}_{\mathrm{met}} = T_{\mathrm{r}}/T\left[[i]_{\mathrm{met}}\left(1 + \frac{\ln(1-[i]_{\mathrm{met}})}{[i]_{\mathrm{met}}} - \frac{1}{1-[\mathrm{I}]_{\mathrm{met}}}\right) - [i]^2_{\mathrm{met}}[\mathrm{I}]_{\mathrm{met}}\left(\frac{1}{1-[\mathrm{I}]_{\mathrm{met}}} + \frac{1}{1-[i]_{\mathrm{met}}} + \frac{[\mathrm{I}]_{\mathrm{met}}}{2(1-[\mathrm{I}]_{\mathrm{met}})^2} - 1\right)\right] \quad (2)$$

for element i = O or S, and $\gamma^{\mathrm{Fe}}_{\mathrm{met}}$ is the activity coefficient for Fe in the liquid alloy calculated by equation (23) of ref. 21, $[i]_{\mathrm{met}}$ is the atomic fraction of S or O present in the metal alloy, and T_{r} is 1,873 K. Quoted uncertainties are 1σ standard errors. Negative coefficients for the X^{i}_{met} terms signify more siderophile partitioning behaviour because X^{i}_{met} correlates negatively with $[i]_{\mathrm{met}}$. The magnitudes of the coefficients associated with the P/T and $X^{\mathrm{S}}_{\mathrm{met}}$ terms are corroborated by a series of piston cylinder experiments (Extended Data Fig. 2, Supplementary Tables 2 and 3).

Application of this parameterization to MORB mantle core formation models yields a $D^{\mathrm{I}}_{\mathrm{met/sil}}$ value of 3.4 ± 1.1 (1σ) (blue circle, Fig. 2a) and confirms that the core can be an important reservoir for bulk Earth I and ^{129}Xe* (ref. 20). This estimate for $D^{\mathrm{I}}_{\mathrm{met/sil}}$ is derived using the P–T–X conditions (38 GPa, 3,500 K) that produce mantle with bulk

[1]Geophysical Laboratory, Carnegie Institution of Washington, Washington DC 20015, USA. [2]Department of Mineral Sciences, National Museum of Natural History, Smithsonian Institution, Washington DC 20560, USA.

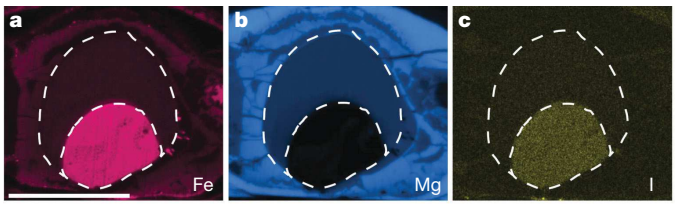

Figure 1 | Compositional maps of Fe, Mg and I from the sample recovered from DAC_I_EXP5, spot 3 at 4,500 K and 40 GPa. a, Fe map; **b**, Mg map; and **c**, I map. The smaller dashed outline in each image surrounds the quenched liquid-Fe alloy, the core-analogue material. The larger dashed outline defines the area of the quenched silicate liquid, the magma-ocean-analogue material. The I in **c** is enriched in core-analogue material and depleted in magma-ocean-analogue material. Maps are taken by energy dispersive spectroscopy (EDS; at 10 kV). Scale bar is 10 μm.

silicate Earth (BSE) values for [FeO] and [W] (Supplementary Table 4), under the endmember scenario that metal segregated from MORB mantle at a temperature along the mantle liquidus[22] and occurred as a single event with complete equilibrium between silicate and metal. Major-element chemistry calculations of core–mantle equilibrium follow the approach of ref. 11, and W partitioning is taken from the parameterization reported in ref. 18. Accounting for $[W]_{BSE}$ and $[FeO]_{BSE}$ in a single-stage core formation model requires a Hf/W_{BSE} ratio between 74 and 93 (3.0–3.8 parts per billion (p.p.b.) W_{BSE}), higher than the current best estimate of 18 for primitive MORB source mantle (Methods, Supplementary Table 4).

Given that I is a siderophile element, different episodes of core formation will create early-forming I/Pu variability, and hence $^{129}Xe^*/^{136}Xe^*_{Pu}$ heterogeneity in the mantle[20] (Fig. 2). A $(2.8 \pm 0.4) \times 1\sigma$ depletion in I for plume mantle would account for the $^{129}Xe^*/^{136}Xe^*_{Pu}$ offset between MORB and plume mantle if both reservoirs synchronously closed to Xe loss[8]. A $D^{I}_{met/sil}$ value of 14.4 ± 2.1 (1σ) is sufficient to deplete I in plume mantle by 2.8× relative to MORB mantle (the uncertainty on I depletion is not propagated to the $D^{I}_{met/sil}$ value) if equal concentrations of I were present during plume and MORB mantle core formation. Larger depletions of I are required to explain the low $^{129}Xe^*/^{136}Xe^*_{Pu}$ ratios of plume mantle if plume mantle closed to Xe loss before MORB mantle did. Smaller depletions are needed if I was present at lower abundances during plume mantle core formation. The fact that I is siderophile under high *P*–*T* conditions (1) removes the need to interpret low $^{129}Xe^*/^{136}Xe^*_{Pu}$ mantle ratios as strictly related to volatile-element depletion during earlier stages of accretion[2–4] and (2) argues against low W anomalies being related to the incorporation of metal into plume mantle[10] because early-forming, high *P*–*T* metal should contain relatively high $^{129}Xe^*/^{136}Xe^*_{Pu}$, opposite to the observations of refs 2–4.

Tungsten becomes less siderophile with increasing *P* along the mantle liquidus and with increasing oxygen fugacity[16–18]. Thus, increasing the *P* for core–mantle equilibration would produce mantle with decreased Hf/W and I/Pu ratios. These parent–daughter fractionations will produce coupled Xe and W anomalies in the mantle with time. We quantify the coupled production of Xe and W anomalies resulting from the partitioning of I and W under a range of *P*–timing conditions for single-stage core formation (Fig. 3a). Partitioning for I follows from equation (1). Core formation chemistry is calculated in a single-stage framework to limit the number of free parameters and to emphasize the direct effects of partitioning[23]. See Methods for additional details regarding the isotopic evolution calculation. The goal here is to identify *P*–timing conditions for core formation where mantle forms with a >2.8× depletion in I and with the most extreme W anomalies observed for plume mantle, both higher and lower than MORB mantle[9,10].

Mantle that conforms to these geochemical requirements experiences core formation under higher *P* conditions and earlier compared to MORB mantle (Fig. 3a). High *P* conditions are required to deplete I and evolve to the lower $^{129}Xe^*/^{136}Xe^*_{Pu}$ ratios associated with plume mantle[2–4,8]. Early metal segregation from plume mantle is required to evolve the observed high and low W anomalies[9,10]. Tungsten isotope evolution in plume mantle follows a two-stage calculation (single-stage core formation). Within the endmember scenario of single, discrete metal segregation events for different mantle reservoirs, the MORB mantle age corresponds to the final step of core formation, and earlier plume mantle ages imply that core formation for these mantle reservoirs occurred before accretion was complete.

Core formation scenarios that successfully account for Xe and W anomalies also produce plume mantle with high FeO contents (Fig. 3). FeO-rich, dense mantle would be robust to mixing with other mantle reservoirs[19], and this may explain why plume mantle preserves isotopic anomalies associated with short-lived decay. High FeO contents are a direct result of the high *P*–*T* metal–silicate equilibrium[11,12] that is required to explain the $>(2.8 \pm 0.4)\times$ depletion in I. A crucial facet to the modelling presented here is that I, a highly volatile element, was present during core formation for both plume and MORB mantle rather than being added only during the late veneer[24] (see Methods for additional discussion).

In addition to being FeO-rich, mantle that experienced core formation under high *P*–*T* conditions would form with elevated abundances of moderately siderophile elements (MSEs), including W, Ni and Co (Extended Data Fig. 3), and high oxygen fugacity[11]. Accordingly, this model predicts positive correlations between the magnitude of W anomalies and the abundances of MSEs in plume mantle. Such correlations have not been resolved, and the potential contribution of plume mantle to the bulk silicate Earth MSE budget is highly variable owing to the uncertainty for plume mantle volume and MSE concentrations (see Methods). We emphasize that plume mantle is dominated by Xe recycled from the atmosphere[2–4]. The presence of this recycled Xe component demonstrates that the geochemistry of plume mantle mostly reflects recycled materials, not accretion processes, and that geochemical correlations associated with accretion will be obscured. The preservation of Xe and W isotopic anomalies may be related to the

Table 1 | Data used to determine the I partitioning parameters in equation (1)

Experiment	Spot number	*P*/*T* (GPa K^{-1})	$[S]_{met}$	$[O]_{met}$	$[I]_{met}$	$\ln(D^{I}_{met/sil})$	$\ln(\gamma^{Fe}_{met})$
DAC_I_EXP1	1	0.006	0.197	0.038	0.005	−0.15	0.01
DAC_I_EXP1	2	0.0074	0.083	0.119	0.009	1.26	0.25
DAC_I_EXP1	3	0.0073	0.341	0.167	0.019	2.03	1.26
DAC_I_EXP3	1 upper	0.0098	0.063	0.055	0.004	0.76	−0.3
DAC_I_EXP3	1 lower	0.0098	0.065	0.107	0.004	0.85	0.09
DAC_I_EXP3	2	0.0103	0.227	0.158	0.018	1.85	0.62
DAC_I_EXP3	3	0.0088	0.258	0.063	0.002	0.92	0.19
DAC_I_EXP5	2	0.0094	0.224	0.275	0.004	1.8	1.36
DAC_I_EXP5	3	0.0088	0.319	0.181	0.005	2.56	0.93
DAC_I_EXP5	4	0.0082	0.3	0.062	0.01	1.47	0.13
DAC_I_EXP8	1	0.0092	0.145	0.298	0.028	2.35	0.91
DAC_I_EXP8	2	0.01	0.189	0.223	0.024	2.21	0.81
DAC_I_EXP9	4	0.0089	0.001	0.044	0.003	−1.14	−0.1
DAC_I_EXP10	2	0.0092	0.001	0.038	0.008	−0.38	−0.11
DAC_I_EXP10	5	0.0076	0.001	0.04	0.006	−0.76	−0.12
DAC_I_EXP11	2	0.0095	0.103	0.192	0.019	1.55	0.83
DAC_I_EXP11	4	0.0081	0.365	0.168	0.015	2.64	1.2
DAC_I_EXP13	2	0.006	0.35	0.191	0.007	−0.29	1.36

Each data category (for example, *P*/*T*) used in equation (1) was identified as significantly correlated with variations in $\ln(D^{I}_{met/sil}) + \ln(\gamma^{Fe}_{met})$ at the 2σ confidence level using an unweighted, stepwise fitting routine. A complete listing of compositional, pressure, temperature, and uncertainty metadata associated with each DAC heating spot is provided in Supplementary Table 1.

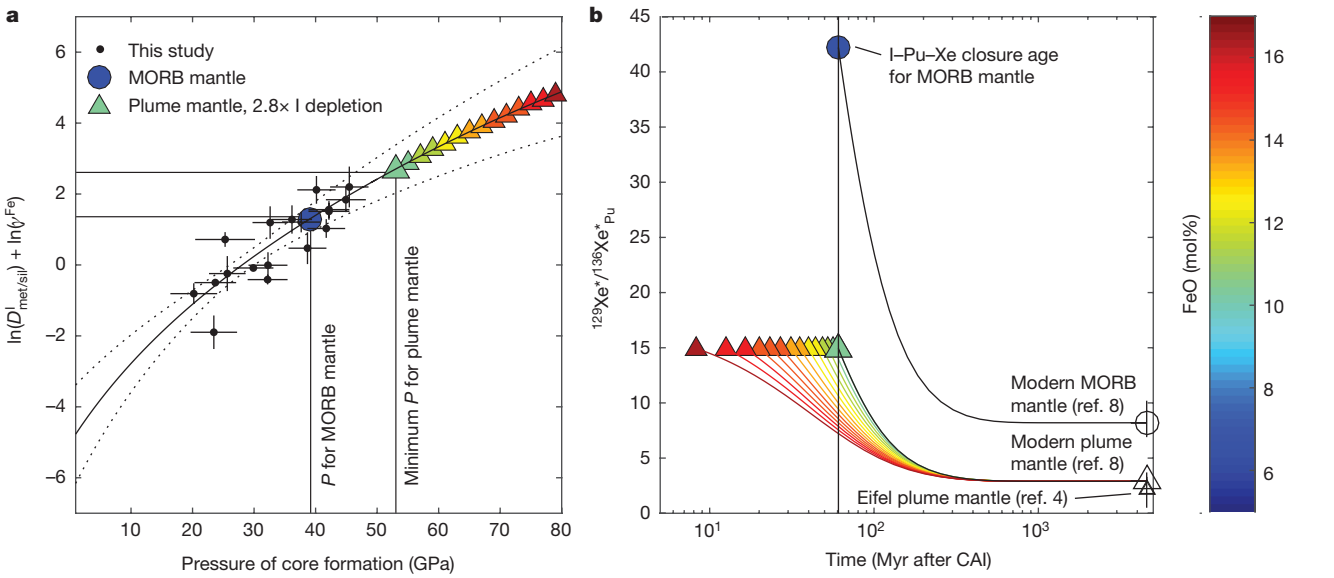

Figure 2 | I partitioning (γ^{Fe}-corrected) during core formation with corresponding Xe isotopic evolution in different mantle domains. **a**, Measured $D^{I}_{met/sil}$ values (dots, 1σ horizontal and vertical uncertainties) from this study are corrected to the mantle liquidus geotherm[22] and O content of the Fe alloy (S-free) in equilibrium with silicate along the liquidus geotherm. Predicted $D^{I}_{met/sil}$ values are plotted as the solid line: equation (1) with associated 1σ uncertainty envelope (dotted lines). **b**, Plume mantle formation scenarios with earlier closure ages require progressively larger depletions of I to account for the larger proportion of undecayed ^{129}I at closure to evolve to the same $^{129}Xe^{*}/^{136}Xe^{*}_{Pu}$ ratio. Vertical lines associated with the black outline symbols on the right-hand axis (for the MORB mantle[8] and the plume mantle[4,8]) are 1σ uncertainties.

fluid mobility of Xe and W during subduction and their corresponding inefficient recycling[2,25].

Linking short-lived isotopic heterogeneity to discrete episodes of core formation implies that Earth's mantle retains a record of the intermediate stages of its growth (Fig. 4). We summarize our model timeline as follows: Earth grew sufficiently large such that I became siderophile under deep-mantle P–T conditions (Fig. 2). Subsections of the mantle then experienced core extraction under relatively high P–T conditions to generate today's I-depleted plume mantle with higher and lower W anomalies (Fig. 3a). The majority of the mantle (MORB mantle) experienced a lower average pressure of metal segregation. Plume and MORB mantle did not homogenize owing to density differences related to their differing FeO contents (Figs 2 and 3), allowing for the ingrowth and preservation of Xe and W anomalies. Our model departs from those in which P–T progressively increases throughout accretion and the entire mantle homogenizes[11,26]. Instead, our model produces an initially heterogeneous mantle consistent with dynamical and observational constraints.

Earth was capable of experiencing earlier stages of high P–T core formation based on several lines of reasoning. Accretion models constrained by the W and Pb isotopic composition of MORB mantle suggest that Earth rapidly accreted to nearly its full size within about 50 million years after the initiation of the Solar System[27] and was therefore capable of producing high pressures before the Moon-forming

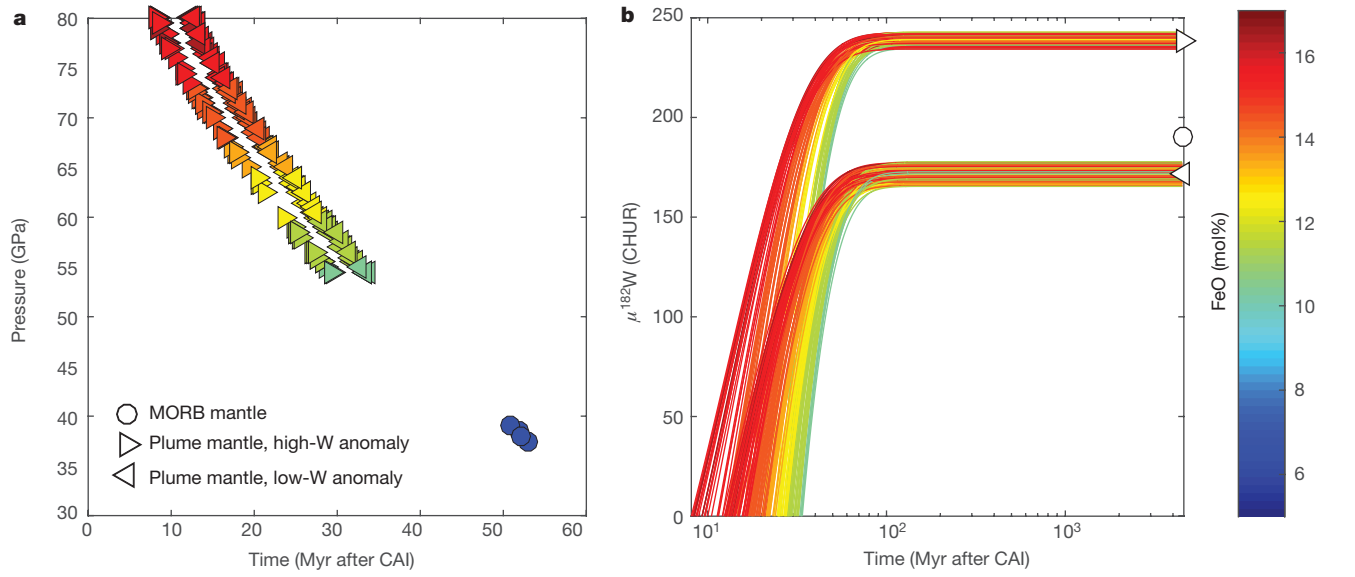

Figure 3 | P–timing conditions of core extraction scenarios that lead to co-evolution of observed Xe and W isotopic anomalies. **a**, Specific modelling targets are as follows: (1) a >2.8× depletion of I relative to MORB mantle and (2) the most extreme observed W isotopic anomalies (right-facing triangles, high anomalies[9]; left-facing triangles, low anomalies[10]). The high P–T conditions associated with plume mantle formation force the FeO content of plume mantle (colour of symbol; see colour bar) to be correspondingly high. **b**, The modelled W isotopic evolution that results from the P–timing conditions that successfully lead to the observed Xe and W anomalies. CHUR, chondritic uniform reservoir.

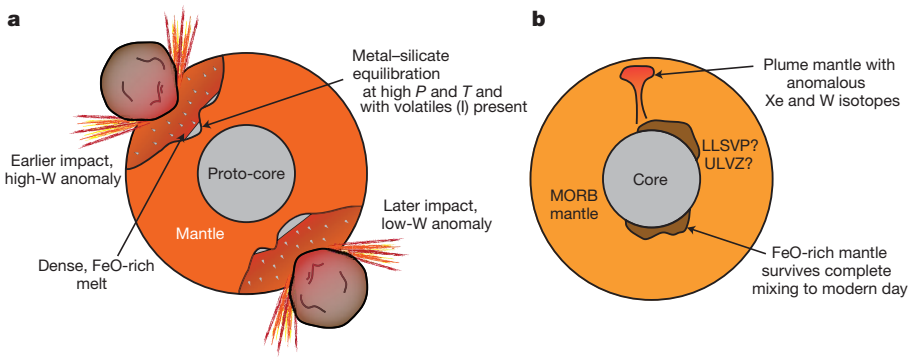

Figure 4 | Cartoon illustrating our model for the co-generation and preservation of Xe and W anomalies. a, Earth experiences multiple large impacts; I and other highly volatile elements are present. FeO-rich silicate liquids are produced via high-*P*, high-*T* metal–silicate equilibration. The high density of these FeO-rich liquids makes them prone to long-term preservation as distinct geochemical reservoirs that experienced core extraction under distinct *P*–*T*–*X* conditions. We suggest that an earlier impact results in a high-W anomaly, and vice versa, because of the timing offsets depicted in Fig. 3. **b**, Potential modern expression of early-forming reservoirs as components within large low-shear-velocity provinces (LLSVPs) and ultralow-velocity zones (ULVZs), which contain materials with relatively low $^{129}Xe^*/^{136}Xe^*_{Pu}$ and variable $^{182}W/^{184}W$.

impact. Energetic impacts that cause deep magma oceans occur throughout accretion[28]. Following each impact, metal–silicate equilibrium would be established over the depth range of the impact-induced magma ocean leading to a range of mantle chemistry. In the deepest portions of the magma ocean, metal–silicate equilibration could occur under very high *P*–*T* conditions such that the silicate liquid is enriched in FeO and gravitationally stabilized against convective mixing with the rest of the mantle (Fig. 4). The less FeO-rich portions of mantle involved in core formation would be more likely to homogenize and comprise MORB mantle.

High *P*–*T* core formation, and the concomitant production of FeO-rich mantle, may also contribute to the formation of large low-shear-velocity provinces and ultralow-velocity zones, which are seismically slow and putatively dense regions of the lowermost mantle usually associated with plume mantle[13,29,30]. In this context we also note that mantle formed under high *P*–*T* conditions, and subsequently stored near the core–mantle boundary, would suffer minimal ^{3}He degassing. This may explain the high ^{3}He/^{4}He ratios that define high-^{3}He/^{4}He (plume) mantle[1,2,14].

Online Content Methods, along with any additional Extended Data display items and Source Data, are available in the online version of the paper; references unique to these sections appear only in the online paper.

Received 22 May; accepted 22 November 2017.

1. Allègre, C. J., Staudacher, T., Sarda, P. & Kurz, M. Constraints on evolution of Earth's mantle from rare gas systematics. *Nature* **303,** 762–766 (1983).
2. Mukhopadhyay, S. Early differentiation and volatile accretion recorded in deep-mantle neon and xenon. *Nature* **486,** 101–104 (2012).
3. Peto, M. K., Mukhopadhyay, S. & Kelley, K. A. Heterogeneities from the first 100 million years recorded in deep mantle noble gases from the Northern Lau Back-arc Basin. *Earth Planet. Sci. Lett.* **369/370,** 13–23 (2013).
4. Caracausi, A., Avice, G., Burnard, P. G., Füri, E. & Marty, B. Chondritic xenon in the Earth's mantle. *Nature* **533,** 82–85 (2016).
5. Moreira, M., Kunz, J. & Allegre, C. Rare gas systematics in popping rock: isotopic and elemental compositions in the upper mantle. *Science* **279,** 1178–1181 (1998).
6. Holland, G. & Ballentine, C. J. Seawater subduction controls the heavy noble gas composition of the mantle. *Nature* **441,** 186–191 (2006).
7. Tucker, J. M., Mukhopadhyay, S. & Schilling, J. G. The heavy noble gas composition of the depleted MORB mantle (DMM) and its implications for the preservation of heterogeneities in the mantle. *Earth Planet. Sci. Lett.* **355/356,** 244–254 (2012).
8. Parai, R. & Mukhopadhyay, S. The evolution of MORB and plume mantle volatile budgets: constraints from fission Xe isotopes in Southwest Indian Ridge basalts. *Geochem. Geophys. Geosyst.* **16,** 719–735 (2015).
9. Rizo, H. *et al.* Preservation of Earth-forming events in the tungsten isotopic composition of modern flood basalts. *Science* **352,** 809–812 (2016).
10. Mundl, A. *et al.* Tungsten-182 heterogeneity in modern ocean island basalts. *Science* **356,** 66–69 (2017).
11. Rubie, D. C. *et al.* Heterogeneous accretion, composition and core–mantle differentiation of the Earth. *Earth Planet. Sci. Lett.* **301,** 31–42 (2011).
12. Frost, D. J., Mann, U., Asahara, Y. & Rubie, D. C. The redox state of the mantle during and just after core formation. *Phil. Trans. R. Soc. Lond.* **366,** 4315–4337 (2008).
13. French, S. W. & Romanowicz, B. Broad plumes rooted at the base of the Earth's mantle beneath major hotspots. *Nature* **525,** 95–99 (2015).
14. Kurz, M. D., Jenkins, W. J. & Hart, S. R. Helium isotopic systematics of oceanic islands and mantle heterogeneity. *Nature* **297,** 43–47 (1982).
15. Kleine, T. *et al.* Hf–W chronology of the accretion and early evolution of asteroids and terrestrial planets. *Geochim. Cosmochim. Acta* **73,** 5150–5188 (2009).
16. Walter, M. J. & Thibault, Y. Partitioning of tungsten and molybdenum between metallic liquid and silicate melt. *Science* **270,** 1186–1189 (1995).
17. Cottrell, E., Walter, M. J. & Walker, D. Metal–silicate partitioning of tungsten at high pressure and temperature: implications for equilibrium core formation in Earth. *Earth Planet. Sci. Lett.* **281,** 275–287 (2009).
18. Wade, J., Wood, B. J. & Tuff, J. Metal–silicate partitioning of Mo and W at high pressures and temperatures: evidence for late accretion of sulphur to the Earth. *Geochim. Cosmochim. Acta* **85,** 58–74 (2012).
19. Sleep, N. H. Gradual entrainment of a chemical layer at the base of the mantle by overlying convection. *Geophys. J. Int.* **95,** 437–447 (1988).
20. Armytage, R. M., Jephcoat, A. P., Bouhifd, M. A. & Porcelli, D. Metal–silicate partitioning of iodine at high pressures and temperatures: implications for the Earth's core and 129* Xe budgets. *Earth Planet. Sci. Lett.* **373,** 140–149 (2013).
21. Ma, Z. Thermodynamic description for concentrated metallic solutions using interaction parameters. *Metall. Mater. Trans. B* **32,** 87–103 (2001).
22. Fiquet, G. *et al.* Melting of peridotite to 140 gigapascals. *Science* **329,** 1516–1518 (2010).
23. Walter, M. J. & Cottrell, E. Assessing uncertainty in geochemical models for core formation in Earth. *Earth Planet. Sci. Lett.* **365,** 165–176 (2013).
24. Wang, Z. & Becker, H. Ratios of S, Se and Te in the silicate Earth require a volatile-rich late veneer. *Nature* **499,** 328–331 (2013).
25. Jackson, M., Shirey, S., Hauri, E., Kurz, M. & Rizo, H. Peridotite xenoliths from the Polynesian Austral and Samoa hotspots: implications for the destruction of ancient ^{187}Os and ^{142}Nd isotopic domains and the preservation of Hadean ^{129}Xe in the modern convecting mantle. *Geochim. Cosmochim. Acta* **185,** 21–43 (2016).
26. Wood, B. J., Walter, M. J. & Wade, J. Accretion of the Earth and segregation of its core. *Nature* **441,** 825–833 (2006).
27. Rudge, J. F., Kleine, T. & Bourdon, B. Broad bounds on Earth's accretion and core formation constrained by geochemical models. *Nat. Geosci.* **3,** 439–443 (2010).
28. Chambers, J. E. & Wetherill, G. W. Making the terrestrial planets: *N*-body integrations of planetary embryos in three dimensions. *Icarus* **136,** 304–327 (1998).
29. McNamara, A. K. & Zhong, S. Thermochemical structures beneath Africa and the Pacific Ocean. *Nature* **437,** 1136–1139 (2005).
30. Jackson, M., Konter, J. & Becker, T. Primordial helium entrained by the hottest mantle plumes. *Nature* **542,** 340–343 (2017).

Supplementary Information is available in the online version of the paper.

Acknowledgements Portions of this work were performed at GeoSoilEnviroCARS (The University of Chicago, Sector 13), the Advanced Photon Source, Argonne National Laboratory. GeoSoilEnviroCARS is supported by the National Science Foundation—Earth Sciences (EAR-1128799) and the Department of Energy—GeoSciences (DE-FG02-94ER14466). This research used resources of the Advanced Photon Source, a US Department of Energy (DOE) Office of Science User Facility operated for the DOE Office of Science by

Argonne National Laboratory under contract number DE-AC02-06CH11357. We acknowledge the support provided by C. Prescher, E. Greenberg, and V. Prakapenka during the experiments conducted at GSECARS and in data reduction. We acknowledge E. Bullock and S. Vitale for their assistance with the electron microscopy, electron microprobe analysis, and focused ion beam recovery. We thank T. Gooding for his assistance in preparing the piston cylinder experiments for analysis. We acknowledge discussions with R. Fischer, R. Parai, S. Parman, J. Tucker and M. Nakajima during the development of the manuscript. C.R.M.J., N.R.B. and Z.D. acknowledge fellowship support from the Carnegie Institution for Science, and C.R.M.J. additionally acknowledges fellowship support from the Smithsonian Institution. The research was also supported by NSF grants to C.R.M.J. (EAR-1725315), to E.C. (EAR-0738654) and to Y.F. (EAR-1447311).

Author Contributions C.R.M.J. conceived the project. C.R.M.J. conducted the experiments and analyses in collaboration with N.R.B. and Z.D. C.R.M.J., N.R.B. and Z.D. all contributed to the model framework. N.R.B. conducted the W isotope and major-element chemistry calculations. C.R.M.J., N.R.B., Z.D., E.C. and Y.F. contributed to data interpretation, presentation and manuscript preparation. E.C. facilitated the project and piston cylinder experiments. Y.F. facilitated the project and DAC experiments.

Author Information Reprints and permissions information is available at www.nature.com/reprints. The authors declare no competing financial interests. Readers are welcome to comment on the online version of the paper. Publisher's note: Springer Nature remains neutral with regard to jurisdictional claims in published maps and institutional affiliations. Correspondence and requests for materials should be addressed to C.R.M.J. (jacksonc3@si.edu).

Reviewer Information *Nature* thanks G. Avice and the other anonymous reviewer(s) for their contribution to the peer review of this work.

METHODS

DAC experiments. *Preparation.* All DAC experiments used pre-indented Re gaskets. Gaskets for experiments under 25 GPa were indented to 35 μm thickness, and gaskets for experiments above 25 GPa were indented to 20 μm thickness. A 130-μm sample chamber was cut into each gasket using a laser drill following indentation. A synthetic silicate–metal mixture with a composition of C1/C[31] was ball-milled and then mixed with 5% KI ± 20% FeS using a mortar and pestle. Given the small size of each laser heating spot, the fact that the entire sample is not melted, and the ubiquitous presence of C, the bulk composition of each laser heating spot is highly variable. These starting materials were loaded into sample chambers and then compressed using stepped anvils machined to the diameter of the sample chamber[32]. The height of the stepped anvils is about 10 μm. The remaining portions of the sample chamber were filled using pressed foils of MgO. This creates a three-layer arrangement with two layers of MgO about 10 μm thick surrounding a silicate–metal mixture approximately 10 μm thick. Gaskets were then loaded into a DAC and placed in a vacuum oven for overnight heating at 110 °C to minimize adsorbed water on sample powders. Immediately after removal from the vacuum oven, gaskets were compressed to moderate pressure. Once the DAC had cooled to room temperature, the gaskets were compressed to the desired experimental pressure. Pressure upon compression was monitored using the diamond edge technique[33].
Laser heating and X-ray diffraction (XRD). DAC sample heating was completed at beamline 13-ID-D of the GSECARS facility at the Advanced Photon Source using a double-sided, flat-top laser heating system ($\lambda = 1{,}064$ nm) with a diameter of about 20 μm. Emission spectra were collected for both sides of the heating spot using light from a 2 μm × 2 μm region co-aligned with the XRD measurements. Temperatures were calculated from the emission spectra, assuming greybody behaviour. Temperatures reported here used light collected between 670 nm and 770 nm. Including longer-wavelength data reduced the quality of fit and generally resulted in lower temperatures (about 200 K). Each reported temperature is the average of a series of measurements taken in rapid succession. At high temperature (>3,000 K), five spectra are taken for each series per side of the heating spot. Temperatures reported for an experiment are the average of the final series of temperature measurements on the hotter of either the upstream or downstream sides. We take the hotter of the two temperatures as there is the potential for small misalignments between the hottest portion of the heating spot and the region where light was collected for the spectral measurement. Any misalignment creates bias towards cooler temperatures. Uncertainties in temperature are the standard deviations (1σ) of the final series of temperature measurements on the hotter side of the DAC plus an analytical uncertainty of 100 K. Heating cycles generally lasted several minutes and heating spots were held at peak or near-peak temperatures for >10 s. Temperatures for DAC experiments are reported in Supplementary Table 1.

XRD data were collected for every heating spot before heating and with every temperature measurement during heating. These data we processed with Dioptas software[34] to calculate pressure before heating ('cold pressure') and pressure during the heating cycle (Supplementary Table 1). We use the unit cell volume of MgO, which was present as the pressure medium in all experiments, to calculate the cold pressure.

The pressure during the heating cycle deviates from the cold pressure owing to relaxation of the sample and thermal expansivity. The combination of these effects generally results in a 10–20% increase in pressure upon heating to melting temperatures at mid-mantle pressures[35].

At high temperatures (>3,000 K) in the experiments reported here, a second set of MgO peaks are present within the XRD spectra. This second set of MgO peaks are shifted towards larger volume compared to the MgO peaks of the pressure medium. We interpret the larger-volume MgO peaks to be the Fe-bearing MgO phase that mantles all heating spots in the present experiments (Fig. 1), and these peaks are used to calculate thermal pressure. To calculate pressure, we apply the volume measurements from the XRD data and the temperature measurements to the thermal equation of state for MgO from ref. 36. This approach neglects the FeO present in the mantling MgO phase (magnesium number Mg# of about 80) and the temperature gradient across the mantling phase. These two effects cancel to a degree. This approach has the advantage of being able to monitor thermal pressure over the duration of the experiment. Uncertainty on the pressure measurement is the fractional uncertainty of the temperature measurement multiplied by the hot pressure plus 2 GPa (Supplementary Table 1).

Heating spots DAC_I_EXP5 spot 4, DAC_I_EXP11 spot 4, and DAC_I_EXP13 spot 2 all have thermal pressure in excess of 30% initial pressure. This is larger than normally attributed to thermal pressure in core formation DAC experiments[37]. We suggest that the large thermal pressure relates to the pre-relaxation of the heating spot due to previous heating spots completed in the same cell.
Chemical analysis preparation. The heating spots of the DAC experiments were prepared for analysis using a focused ion beam (30 kV, Ga^+ ions, Auriga, Zeiss Instruments) at Carnegie Institution for Science, Washington DC following the technique of ref. 38. Samples were milled to expose a cross-section of the heating spot parallel to the laser beam used to heat the sample. Milling proceeded on each heating spot until quenched metal and quenched silicate phases were exposed and the exposure of the metal phase had nearly reached its full diameter. The final milling step was completed with a 2-nA beam to prepare a flat surface for wavelength dispersive spectroscopy analysis and EDS mapping.
Piston cylinder experiments. *Preparation.* A series of piston cylinder experiments were conducted at the Department of Mineral Sciences, National Museum of Natural History, USA, to corroborate the DAC results. Experiments were run using 0.5-inch-diameter assemblies, comprising $BaCO_3$ pressure media wrapped in Pb foil, straight-walled graphite heaters, and MgO spacers. Temperatures were monitored using a D-type thermocouple housed in a four-hole alumina rod inserted axially into the assembly. MgO spacers were machined to position the hotspot between the sample capsule and the thermocouple junction. Starting materials were oxide and carbonate powders mixed to generate a basaltic composition (62A from ref. 39). This powder was decarbonated and reduced to the oxygen fugacity of mostly iron–wüstite (IW) at 1,373 K overnight. Following decarbonation and reduction, the oxide was then mixed with either FeNiSi alloy, FeSi alloy, FeSi + FeS or Fe + FeS to yield a 50:50 silicate–metal mixture by weight. I was added as KI, AgI or I to yield approximately 4 wt% I in the starting material. Graphite capsules were used in all experiments. Capsules were isolated from the graphite heater by an Al_2O_3 sheath, and the thermocouple was isolated from the graphite capsule by a 1-mm-thick disk of MgO.

Samples were cold-compressed to 1 GPa. Following compression, sample temperatures were ramped to 1,073 K and allowed to sinter for 2 h. Experiments were then ramped to 1,973 K and held at that temperature for 20–40 min. Experimental pressures were 1.5 GPa.
Chemical analysis preparation. Piston cylinder experiments were prepared to minimize the loss of fluid-mobile components from the run products. A basaltic silicate composition was chosen to enable the silicate to quench to a glass. Graphite capsules were sectioned using a diamond wafering blade without lubrication. Initial exposure of run products was completed with SiC sandpaper using Turbinoid as a lubricant. Final polishing was completed using alumina-impregnated sheets without lubricant.

A series of piston cylinder experiments were run and prepared with water-based lubrication. In these experiments, I-rich materials were observed on the polished surfaces following the final polishing step. We do not report these experiments because of the clear mobility of I before analysis.
Chemical analysis. Chemical analyses were completed using a JEOL 8530F field-emission microprobe at the Carnegie Institute for Science. Analyses of metal phases were performed with a beam diameter ranging from a focused beam to a 2-μm-diameter beam. Analyses on silicate materials were conducted with a 1-μm-diameter beam. All analyses employed a 10-kV accelerating voltage and 2–10-nA beam current. Repeated analyses of the same material with different current densities yielded no evidence for the volatilization of I during microanalysis. Analytical standards for silicate analyses were ENAL5 (enstatite stoichiometry glass with 5 wt% Al_2O_3, for Mg, Si and Al), basalt 812 glass (for Ca, K, Fe), FeS_2 (for S), and KI (for I). Analytical standards for metal analyses were ENAL5 (for Mg, Si and Al), basalt 812 glass (for Ca and K), FeS_2 (for S), KI (for I), Fe_7C_3 (for C and Fe), and Fe_3O_4 (for O). The Fe_7C_3 standard was synthesized following the method outlined in ref. 40. Multiple analyses were conducted on the silicate phase and metal phase contained within each heating spot. Analytical uncertainties are calculated as standard errors of the repeat analyses of a given material. Standard errors are reported because the quench textures of metals and silicate can be coarse with respect to the beam diameter. Heating spots with small metallic phases were analysed and repolished with the focused ion beam to allow for repeat analyses. Reanalysis of metals without polishing resulted in analyses with carbon concentrations about 1 wt% higher compared to the original analysis.

The glass phases of the piston cylinder experiments were analysed using the same routine developed for the silicate phases in the DAC. The metallic phases of the piston cylinder experiments were analysed with a 15-kV accelerating voltage and 50-nA beam current, with the beam defocused to 10 μm, to achieve a lower detection limit for I. Standards were the same as the 10-kV routine with the following additions: Ag metal (Ag), basalt 812 glass (Na and Ti), Ni-olivine (Ni), MnO_2 (Mn) and chromite (Cr). All samples and standards were coated with Ir to prevent charging and facilitate the quantification of C in metal.

The compositions of DAC experimental products are reported in Supplementary Table 1, and the compositions of piston cylinder experimental products are reported in Supplementary Table 2.
Data processing and fitting. To parameterize $D^{I}_{met/sil}$ values we consider the dissolution partitioning reaction: $[I]_{sil} = [I]_{met}$. We take this partitioning reaction as opposed to other potential reactions because the speciation of I dissolved in liquid Fe alloy and silicate is not known. The partitioning reaction has an associated equilibrium constant, K_I.

$$K_I = \gamma^I_{met}[I]_{met} / \gamma^I_{sil}[I]_{met} \quad (3)$$

$$-K_I = \exp\left(\frac{\Delta H^o}{RT} - \frac{\Delta S^o}{R} + \frac{P\Delta V^o}{RT}\right) \quad (4)$$

where γ denotes the activity coefficient, and [ ] denotes the concentration of a given component. ΔH^o, ΔS^o and ΔV^o are the enthalpy, entropy and volume change of the partitioning reaction for a given pressure and temperature. Assuming ΔH^o, ΔS^o and ΔV^o are constant across the pressure and temperature range of interest and that γ^I_{sil} is a constant, the I partition coefficient ($D^I_{met/sil} = [I]_{met}/[I]_{sil}$) can be expressed as follows:

$$\ln(D^I_{met/sil}) + \ln(\gamma^I_{met}) = a + \frac{b}{T} + \frac{cP}{T} \quad (5)$$

where a, b and c are fitting parameters that scale with ΔS^o, ΔH^o and ΔV^o, respectively. Following from equation (24) in ref. 21, γ^I_{met} is expanded as:

$$\ln(\gamma^I_{met}) = \ln(\gamma^{Fe}_{met}) + \ln(\gamma^{I_o}_{met}) - \sum \varepsilon^i_I X^i_{met} \quad (6)$$

where $\gamma^{I_o}_{met}$ denotes the activity coefficient of I at infinite dilution and ε are the fitted interaction parameters. The sigma terms sum across the alloying components in Fe alloy and X^i_{met} takes the form:

$$X^i_{met} = T_r/T\left[[i]_{met}\left(1 + \frac{\ln(1-[i]_{met})}{[i]_{met}} - \frac{1}{1-[I]_{met}}\right) - [i]^2_{met}[I]_{met}\left(\frac{1}{1-[I]_{met}} + \frac{1}{1-[i]_{met}} + \frac{[I]_{met}}{2(1-[I]_{met})^2} - 1\right)\right] \quad (7)$$

for i = S, C, O or Re and the reference temperature T_r = 1,873 K.

$$X^I_{met} = (T_r/T)\ln(1-[I]_{met}) \quad (8)$$

Known terms are collected on the left and unknown terms are collected on the right, to yield the final expression used for parameterization:

$$\ln(D^I_{met/sil}) + \ln(\gamma^{Fe}_{met}) = a + \frac{b}{T} + \frac{cP}{T} + \sum \varepsilon^i_I X^i_{met} \quad (9)$$

Variations in $\ln(D^I_{met/sil}) + \ln(\gamma^{Fe}_{met})$ were fitted in a stepwise, unweighted least-squares approach. The stepwise matrix includes the $1/T$, P/T, X^I_{met}, X^S_{met}, X^C_{met}, X^O_{met} and X^{Re}_{met} terms. The a term accounts for $\Delta S^o/R$ and is forced to be part of the parameterization.

In the first fitting step, the most significant term is X^O_{met} (with a P value of 0.00005, Extended Data Fig. 1a). Following the addition of X^O_{met}, the most significant term is X^S_{met} (with a P value of 0.02), and following the addition of X^S_{met}, the most significant term is P/T (with a P value of 0.007). No additional terms are significant at the 95% confidence threshold and are therefore not included in the predictive expression for I partitioning (equation (1)). Each step of the stepwise regression is plotted in Extended Data Fig. 1. The fact that X^I_{met} is not significant in the stepwise fitting approach suggests that I doping levels are not high enough to significantly affect $\ln(D^I_{met/sil})$ values; that is, doping levels are within the Henrian regime. The activity coefficient of I at infinite dilution (equation (5), $\gamma^{I_o}_{met}$) in liquid Fe metal is not explicitly accounted for in calculating the solution behaviour of I. This term has the same $1/T$ dependence as the b term, which is not deemed significant and is therefore not included in the current parameterization. The parameter values and the associated covariance matrix are included as Supplementary Table 3. Covariance plots of parameterization terms are provided in Extended Data Fig. 1.

All silicate and metal data were converted to atomic fractions to calculate $D^I_{met/sil}$. Oxygen was subtracted from the silicate analyses according to the valence state of the anionic species, S^{2-} and I^-.

Atomic data were converted to molar oxide for the silicate phase of each experiment to calculate oxygen fugacity and exchange coefficients. The substitution of S and I for O is not accounted for in this conversion. The atomic fraction of S relative to Fe in experiments is approximately 0.1. Correspondingly, any reduction to the mole fraction of FeO that is due to Fe complexing with S is small.

Oxygen fugacity for each experiment was calculated with respect to the iron–wüstite oxygen buffer as:

$$\Delta IW = 2\log_{10}(X^{FeO}_{sil}\gamma^{FeO}/X^{Fe}_{met}\gamma^{Fe}_{met}) \quad (10)$$

We take the expression from ref. 41 for $\ln(\gamma^{FeO}_{sil})$:

$$\ln(\gamma^{FeO}_{sil}) = 2,096/T - 2.6024X^{FeO}_{sil} + 2.2105X^{SiO_2}_{sil} + 0.238X^{CaO}_{sil} - 0.9666 \quad (11)$$

Calculating $\ln(\gamma^{Fe}_{met})$ requires an understanding of how different components interact in liquid Fe alloy, and we follow the formalism for calculating γ^{Fe}_{met} outlined in ref. 21. Non-Fe components in the alloy are limited to O, S and C. Interactions are calculated using the ε values tabulated in the Steelmaking Data Sourcebook[42]. We do not account for I, Re, Mg, K and Al interactions in calculating γ^{Fe}_{met}. These elements are present at minor to trace levels, except for Re, which is present at an atomic fraction of about 0.15 in the metallic phases of three heating spots. Values of γ^{Fe}_{met} were also calculated using the METALACT calculator (MetalAct, http://www.earth.ox.ac.uk/~expet/metalact/; ref. 43) with Si, S, O, C and Re interactions. There is good agreement between the two sets of calculations (not shown).

Low totals in the silicate of DAC heating spots. Several heating spots yielded low totals during analysis of the silicate (DAC_I_EXP5 spot 2, DAC_I_EXP5 spot 4 and DAC_I_EXP11 spot 4; Supplementary Table 1). Following the analysis of DAC_I_EXP5 spot 2 and DAC_I_EXP5 spot 4, vesiculation of the silicate was observed (Extended Data Fig. 4). We interpret this to indicate that the quenched silicate phases in these heating spots were volatile-rich. Low totals during analysis of DAC_I_EXP11 spot 4 may relate to sample specific geometry issues. Ferropericlase and bridgmanite mineral grains were analysed in the region immediately surrounding heating spots with low totals (DAC_I_EXP5 spot 2, DAC_I_EXP5 spot 4 and DAC_I_EXP11 spot 4; not reported). These analyses consistently yielded higher totals than the quenched silicate. This provides additional evidence that the low totals may be related to unanalysed volatiles and are not likely to be related to geometric issues or analytical routine issues.

We note that changes to the major element compositions of ultramafic melts do not appear to have substantial effects on metal–silicate partition coefficients. Following other studies[43], we assume ultramafic melt composition does not affect metal–silicate partition coefficients. The effects of C and H dissolved in ultramafic melts have not been quantified, but we assume from the results with major elements that C and H do not affect partitioning behaviour.

Evaluating equilibrium in DAC experiments. The approach to equilibrium in the present experiments is evaluated by (1) comparing the exchange systematics of the present experiments to previously reported data and (2) reviewing the internal systematics of the present experiments.

Extended Data Fig. 5a compares measurements of Si–Fe exchange coefficients between silicate and metal (K^{Si-Fe}_D) from the present experiments to K^{Si-Fe}_D values compiled by ref. 38. We choose K^{Si-Fe}_D for comparison because it has a high and well-defined temperature dependence and because the compositional effects are relatively small and well constrained[37]. Data from this study have been corrected for Si–Si, Si–O, Si–C and Si–S interactions, and data from the literature have been corrected for Si–Si, Si–O and Si–C interactions. Corrections for Si–Si, Si–C and Si–S were made using the ε parameters reported in ref. 42. Corrections for Si–O were made using the ε parameter reported by ref. 37. Reported and literature K^{Si-Fe}_D values show good correspondence (Extended Data Fig. 5a), suggesting that we heated our samples stably for long enough to closely approach chemical equilibrium and to obtain accurate temperature calculations.

The Mg/Si ratio of eutectic melts in the MgO–$MgSiO_3$ system increases with pressure up to 45 GPa (ref. 44; Extended Data Fig. 5b). This behaviour provides a check on pressure estimates for individual heating spots. Circle symbols are from this study and are binned into three groups by Mg#. Darker symbols denote a lower Mg#. Silicate Mg# spans from 61 to 77. Square symbols have a Mg# of 100 and are from ref. 44.

Compared to the silicate compositions of MgO–$MgSiO_3$ eutectic melts reported by ref. 44 at 35 GPa and 45 GPa (Extended Data Fig. 5b), the silicate liquids from this study have uniformly higher (Mg + Fe)/Si ratios at similar pressures. More FeO-rich silicate liquids within a given pressure range also plot towards higher (Mg + Fe)/Si ratios. These behaviours are expected for systems of similar pressure but variable FeO content. The addition of FeO to a system lowers the melting point of MgO relative to $MgSiO_3$, shifting the eutectic towards MgO. Further support for the pressure calculation comes from the similar slopes of (Mg + Fe)/Si versus pressure for the Mg# groups (symbols of same colour) and the eutectic melt slope[44].

Mobility of I during sample preparation. Experiments conducted with a DAC were prepared for analysis exclusively using a focused ion beam. No contact was made between the samples and a fluid that may promote I mobilization. Nonetheless, many DAC samples developed I-rich blebs in the vicinity of the exposed heating spots during storage in desiccators (Extended Data Fig. 6). Heating spots were analysed using EDS before their removal from the focused ion beam (before the appearance of I-rich blebs). The I contents of the metals and silicates before and after the appearance of I-rich blebs are indistinguishable. This indicates

that the I-rich blebs were not derived from the silicate or metal phases and that the I-rich blebs did not modify the I content of the silicate and metal phases.

EDS analyses of the I-rich blebs indicate that they are rich in Fe, C, I and O. In DAC experiments without S, a material with a similar composition mantles the metal phases (Extended Data Fig. 6) and can extend into the region immediately surrounding the heating spot. We consider this material to be a phase that is separate to the metal and silicate phases. If this I-rich material exsolved from the metal or silicate during quenching in the S-free experiments (the mantling phase is not present in S-bearing experiments), this would imply a very O-rich and I-rich metal or silicate. This possibility is not supported by the partitioning behaviour of O and I in S-bearing experiments. Specifically, I partitioning for S-free experiments is well predicted by S-bearing experiments, and O solubility in metals from S-free experiments is similar to those measured in S-bearing experiments. Moreover, the fact that I-rich blebs are not always observed in direct contact with the silicate or metal phase of a heating spot suggests an independent origin for the I-rich material (Extended Data Fig. 6).

Comparison of DAC and piston cylinder results. A series of piston cylinder experiments were completed to validate the $\ln(D^{I}_{met/sil})$ expression derived using the DAC results (equation (1)). All experiments were conducted at 1.5 GPa and 1,973 K. In all but two experiments the concentration of I in the metal phase was below the detection limit, precluding the quantification of $\ln(D^{I}_{met/sil})$ values. For the analytical parameters (15 kV, 50 nA, 60 s/30 s peak/off-peak counting time) used to measure I in metals of the piston cylinder experiments, the detection limit is 0.006 wt% or 60 parts per million. We take the detection limit to calculate upper limits on $\ln(D^{I}_{met/sil})$ values for these experiments (Extended Data Fig. 2).

I partition coefficients were quantified for two S-bearing piston cylinder experiments. The S-bearing experiments contained two, immiscible metallic liquids; one S-rich and the other S-poor. I is detectable only in the S-rich metallic phase, consistent with S in metallic liquids increasing $\ln(D^{I}_{met/sil})$ values (equation (1)). The two S-bearing experiments were conducted at $\Delta IW - 4.7$ and $\Delta IW - 1.9$, where $\Delta IW + a$ is fugacity in log units relative to the iron–wüstite oxygen buffer. The more reduced experiment yielded a $\ln(D^{I}_{met/sil})$ value that is lower than the predicted range for $\ln(D^{I}_{met/sil})$ at low pressure (95% confidence threshold, Extended Data Fig. 2a). The more oxidized experiment yielded a higher $\ln(D^{I}_{met/sil})$ value that is within the predicted $\ln(D^{I}_{met/sil})$ range. Oxygen fugacity (f_{O_2}) in the DAC experiments averaged $\Delta IW-1.3$, similar to the more oxidized piston cylinder experiment ($\Delta IW-1.9$). Thus, the piston cylinder experiments provide independent support for the predictive ability of the DAC regression for systems with similar f_{O_2}. The fact that the measured $\ln(D^{I}_{met/sil})$ values and upper limit $\ln(D^{I}_{met/sil})$ values plot mostly near the lower limit of the uncertainty envelope favours models with larger P/T terms and lower intercepts (Extended Data Fig. 2b).

From the two piston cylinder experiments, there is preliminary support for oxidizing conditions promoting I partitioning into metallic liquids. This behaviour is consistent with that of other anionic species in core-forming environments[45–48]. Taking the two piston cylinder experiments with measurable I in the metallic phase as a guide for how $\ln(D^{I}_{met/sil})$ scales with f_{O_2} allows the piston cylinder data to be corrected to the average f_{O_2} of the DAC experiments ($\Delta IW-1.3$). The f_{O_2}-corrected piston cylinder data are plotted in Extended Data Fig. 2b.

We choose not to include an f_{O_2} term in the DAC data regression because (1) we apply equation (1) under f_{O_2} similar to the DAC data, (2) the f_{O_2} term is not statistically significant (P value > 0.05) within the stepwise fit of the DAC data, and (3) a systematic study quantifying the relationship between f_{O_2} and $\ln(D^{I}_{met/sil})$ has not been completed.

Modelling Xe and W isotope evolution. *Establishing the I/Pu fractionations required to produce $^{129}Xe^*/^{136}Xe^*_{Pu}$ variability between MORB and plume mantle.* The pertinent isotopic observations comparing Xe isotopes in MORB and plume mantle are as follows: MORB and plume mantle $^{129}Xe^*/^{136}Xe^*_{Pu}$ values are $8.2^{+2}_{-1.3}$ and $2.9^{+0.4}_{-0.1}$, respectively[8], that is, the $^{129}Xe^*/^{136}Xe^*_{Pu}$ ratio for MORB mantle is $2.8 \pm 0.4\times$ higher than in plume mantle. We note the uncertainties in MORB and plume mantle $^{129}Xe^*/^{136}Xe^*_{Pu}$ values are similarly asymmetric such that their ratio has symmetric uncertainty at the precision of the measurements. Isotopic variability within $^{129}Xe^*/^{136}Xe^*_{Pu}$ reflects a combination of different Xe closure ages for plume and MORB mantle and the I/Pu ratios of these two reservoirs during the lifetime of the parent isotope. The Xe closure age (I–Pu–Xe) is the age at which a reservoir starts to accumulate radiogenic Xe related to I and Pu decay. Closure age is calculated as:

$$t^{closure}_{129/244} = (1/\lambda_{244} - \lambda_{129})\ln\left(\frac{^{129}Xe^*}{^{136}Xe^*_{Pu}} \times \frac{^{238}U_i}{^{127}I_i} \times \frac{^{244}Pu_i}{^{238}U_i} \div \frac{^{129}I_i}{^{127}I_i} \times Y_{244}\right) \quad (12)$$

where $^{129}Xe^*/^{136}Xe^*_{Pu}$ is determined for different geochemical reservoirs using average carbonaceous chondrite (AVCC) values for initial mantle Xe (taken from ref. 8) and the remaining parameters are reported in ref. 49. We use the AVCC-based calculations because AVCC provides the best fit[4] to the non-radiogenic components to mantle Xe. The ^{127}I contents of MORB mantle are updated to reflect the most recent estimates[50] of 7 ± 3 p.p.b. I for the bulk silicate Earth.

If MORB and plume mantle closed to Xe loss with the same I/Pu ratios, then MORB mantle must have closed to Xe loss about 30 million years earlier than plume mantle to account for its $2.8\times$ higher ratio of $^{129}Xe^*/^{136}Xe^*_{Pu}$ (Extended Data Fig. 7a). The apparent common heritage of the W isotopes of MORB mantle and the Moon[51,52], however, suggests that MORB mantle closed to Xe loss after the plume mantle did. Lowering the I/Pu ratio of plume mantle progressively lowers its Xe closure age. Equal Xe closure ages for plume and MORB mantle are accounted for if the plume mantle closed with a $2.8\times$ lower I/Pu ratio compared to MORB mantle (Fig. 2b). Greater depletions of I/Pu for plume mantle translate to Xe closure ages that predate Xe closure in MORB mantle (Fig. 2b).

We note that the radiogenic component of the $^{129}Xe/^{130}Xe$ ratio for plume mantle, corrected for recycling, is also approximately $3\times$ lower than MORB mantle (Extended Data Fig. 7b, Supplementary Table 4). The radiogenic component of the $^{129}Xe/^{130}Xe$ ratio is calculated as follows:

$$^{129}Xe/^{130}Xe_{radiogenic} = {}^{129}Xe/^{130}Xe_{mantle-recycling-corrected} - {}^{129}Xe/^{130}Xe_{initial} \quad (13)$$

where $^{129}Xe/^{130}Xe_{initial} = 6.286$ (ref. 49). The similar offsets for $^{129}Xe/^{130}Xe_{radiogenic}$ and $^{129}Xe^*/^{136}Xe^*_{Pu}$ between plume and MORB mantle imply that they are related to the behaviour of I, and not Pu or Xe, during accretion.

Developing W isotopic targets. Xenon from MORB mantle and plume mantle is dominantly from the atmosphere[2–4,6–8]. The injection of atmospheric Xe into the mantle occurs during subduction of slab materials that have interacted with oceanic waters. These materials contain W from the MORB mantle, and therefore, the injection of atmospheric Xe into the mantle also contains a component of MORB W. The MORB mantle $^{182}W/^{184}W$ ratio is not affected by this process, but backmixing MORB W into plume mantle will dilute any $^{182}W/^{184}W$ anomaly present in plume mantle and change its concentration of W.

The degree that plume $^{182}W/^{184}W$ anomalies are diluted owing to backmixing of MORB W depends on the coupling between Xe and W during their respective deep cycles. Both W and Xe are efficiently stripped from the slab because they are incompatible in mantle and slab minerals and fluid that is mobile during slab subduction[53–55]. Alteration of oceanic crust results in a net uptake of Xe into the slab before subduction, increasing Xe concentrations in oceanic crust by $100\times$ to $100{,}000\times$ over Xe concentrations in MORB mantle[56–60].

The W/Th ratio for arc lavas affected by slab melts is essentially equal to the W/Th ratio for MORB[61]. Given that W and Th are incompatible during slab melting, the equality of W/Th in the slab melt and in MORB suggests minimal uptake or loss of W during hydrothermal alteration of oceanic crust. Assuming a $10\times$ increase in [W] for oceanic crust over MORB mantle (10% mantle melting), the slab crust enters the subduction zone with an elevated Xe/W ratio that is $10\times$ to $10{,}000\times$ greater than in MORB mantle. Tungsten and Xe are both mobile during subduction[53–55], but the relative efficiency of Xe and W removal from the slab during dehydration and melting is not known. Because of this uncertainty and the uncertainty on Xe/W ratios of plume mantle, we take the modern $^{182}W/^{184}W$ anomalies as the targets for modelling the isotopic evolution of plume mantle (no W dilution).

Calculation of W and Xe isotopic anomalies resulting from discrete stages of core formation. To identify scenarios where the short-lived isotopic signatures observed in plume and MORB mantle can be generated, we modelled the $^{182}W/^{184}W$ evolution and I depletion of mantle reservoirs that experienced single-stage core extraction at different P–T–X–timing conditions. We calculate core formation as a single-stage process to limit the number of free parameters within each calculation[23] and to facilitate P–T–X–timing comparisons between model outputs. Calculations of major-element chemistry resulting from core formation follow the approach of ref. 11, in which the following mass balance equation is solved:

$$[(FeO)_x(NiO)_y(SiO_2)_z(Mg_uAl_mCa_n)O]_{mantle} + [Fe_aNi_bO_cSi_d]_{core}$$

$$\rightarrow \left[(FeO)_{x'}(NiO)_{y'}(SiO_2)_{z'}(Mg_uAl_mCa_n)O\right]_{mantle} + [Fe_{a'}Ni_{b'}O_{c'}Si_{d'}]_{core} \quad (14)$$

where a, b, c, u, m, n, x, y and z are defined by the composition of the starting material, and a', b', c', x', y', z' are unknowns determined on the basis of the partitioning of Ni, Si and O at the chosen P–T conditions. The starting material used for all calculations is an average of the 'oxidized' and 'reduced' impactor compositions given by ref. 11. A full description of the procedure used for the major-element calculations can be found in ref. 11. This approach has the advantage of coupling the P–T conditions of core formation with the mantle FeO content, an important constraint in our definition of successful model conditions. Partition

coefficients for I are calculated from equation (1). Note that the activity coefficient of Fe in liquid Fe alloy under the applicable T–X conditions is very close to 1 ($\ln(\gamma^{Fe}_{met}) = 0$) and can be neglected in applying equation (1) to natural conditions. Tungsten partitioning is given by ref. 18 and takes the following form:

$$\log(D^{W}_{met/sil}\ (wt\%)) = 1.85 - 6,728/T - 77 \times (P/T) + 3\log(D^{Fe}_{met/sil}\ (wt\%)) \quad (15)$$

A Monte Carlo approach is employed to search the parameter space, in which pressure and the timing of the core formation event are selected at random. Temperature at the chosen pressure is constrained to lie on the peridotite liquidus determined by ref. 22. The distribution of W and I between core and mantle is calculated from the given expressions for partitioning (equation (1) for I and using ref. 18 for W) applying the core–mantle chemistry calculated following ref. 11 (equation (14)). The evolution of the mantle W isotope composition subsequent to the core-forming event is then calculated using the following expression from ref. 62:

$$\mu^{182}_{W\ (CHUR)}(t) = Q_W\left(\frac{^{180}Hf}{^{182}Hf}\right)_{t_0} f^{Hf/W}(e^{-\lambda t_{2stage}} - e^{-\lambda t}) \quad (16)$$

where $\mu^{182}_{W\ (CHUR)}(t)$ is the parts per million deviation in the mantle W isotope composition at time t relative to CHUR, Q_W is related to $^{180}Hf/^{182}W$ of CHUR at $t = 0$, $f^{Hf/W}$ is the enrichment in Hf/W relative to CHUR that results from core formation, and t_{2stage} corresponds to the time after Solar System formation of the core-forming event being considered.

Our initial goal was to use the model to determine the conditions of core-formation that are compatible with the composition of the MORB source reservoir, where this reservoir is approximately comprised of bulk silicate Earth. Models were considered successful when they matched [W][63], [FeO] and the isotopic composition of the bulk silicate Earth[15] (Supplementary Table 4). Our Hf–W age determination of core segregation from MORB mantle occurs later in the accretion timeline than do previous determinations[15]. This difference stems from our requirement to satisfy $[FeO]_{BSE}$, in addition to $[W]_{BSE}$ and $^{182}W/^{184}W$ in the Hf–W calculation. The mutual satisfaction of $[FeO]_{BSE}$ and $[W]_{BSE}$ in a single-stage core formation framework is only possible at the lower end of $[W]_{BSE}$ estimates[63], which forces the Hf–W age to about 50 million years after the initiation of the Solar System (approximately the time of condensation of calcium-aluminium-rich inclusions, CAI) (Fig. 3). Satisfying only $[W]_{BSE}$ yields a Hf–W age of about 30 million years after CAI[15], but the $[FeO]_{BSE}$ implied by this calculation exceeds observations. To calculate the value of $D^{I}_{met/sil}$ applicable to the core-forming event responsible for creating MORB source mantle, we employed the P–T conditions found by averaging the conditions of the successful models described above. Additional discussion of modelled $[W]_{BSE}$ is provided in the Methods subsection 'Collateral geochemical consequences'.

In the second step of the model we search the P–timing parameter space (T is fixed along the liquidus of ref. 22) to identify core extraction scenarios that produce a mantle reservoir with $\mu^{182}W$ values that are low or high relative to those of MORB source mantle by the amounts listed in Supplementary Table 4. In these model calculations, the measured $\mu^{182}W$ anomalies[9,10] are the only constraint that must be satisfied in order to consider the result a success. These core-forming events are those considered further as candidates for the formation of plume mantle. Using the P–T conditions from these successful results, we calculate I partition coefficients and the corresponding depletions in mantle I that result from core extraction. Cases where the calculated I depletion is $\geq 2.8\times$ the value predicted for MORB source mantle are considered successful for both W and Xe isotopes and are plotted in Fig. 3a.

Dynamical simulations of planetary accretion suggest that the majority of volatile elements were delivered to Earth in the final 30% of growth[64]. Relative I depletion between different sections of mantle (plume mantle and MORB mantle) in our model, however, is only a function of core formation. Our model explains I depletion in plume mantle without invoking early accretion of volatile-poor material. If the material that accreted to generate plume mantle was in fact volatile-depleted, it would reduce the pressure required for segregation of core metal from plume mantle (lower $D^{I}_{met/sil}$) and would allow for segregation later in Solar System history (Fig. 3a).

As noted above, the $^{129}Xe^*/^{136}Xe^*_{Pu}$ and $^{129}Xe/^{130}Xe_{radiogenic}$ offsets between plume and MORB mantle both require plume mantle I/Pu and I/Xe ratios to be approximately $3\times$ lower than MORB mantle upon formation. Given the differing volatilities of I, Pu and Xe, the I/Pu and I/Xe ratios of materials accreted to Earth should vary but to different degrees for materials with different volatile contents. This suggests that volatile delivery may have been roughly constant during the period overlapping plume mantle and MORB mantle core formation.

Plutonium, Hf and Xe are assumed not to enter the core in these calculations. Partitioning of Xe and other noble gases into the core has been studied by many groups and their uniform conclusion is that noble gases are not siderophile[65–67], at least across the P–T–X conditions explored so far. Xenon partitioning data have only been reported between 0.5 GPa and 6 GPa and show a negative correlation with increasing pressure, with $D^{Xe}_{met/sil}$ values decreasing from about 0.1 to about 0.001 over this pressure range[66]. We assume that Xe remains lithophile ($D^{Xe}_{met/sil} < 1$) across the P conditions considered here (up to 80 GPa). Partitioning of Pu during core formation has not been directly studied, but other actinides remain lithophile under the P–T–X conditions applicable to core formation in deep magma oceans[68].

We do not require that the calculated Xe closure age be the same as the timing of core extraction for MORB or plume mantle. Xenon closure ages depend on assumptions made for the abundance of I in bulk silicate Earth and assumptions regarding retention of Xe before complete closure. Moreover, both single-stage core formation and Xe closure calculations are idealized scenarios and do not yield ages with absolute chronological meaning. These assumptions make it difficult to directly compare the timing of core extraction and Xe closure ages.

We do not explore the independent effects on W partitioning related to oxygen fugacity (bulk oxygen content of the core–mantle system), S, C or temperatures removed from the mantle liquidus[22]. More reduced, C-rich, and S-poor core formation would make W more siderophile[16–18] and vice versa. Combined, these effects would expand the P–T–timing space (Fig. 3a) for successful W isotopic solutions.

Collateral geochemical consequences. High-pressure metal–silicate equilibrium would cause mantle to form with elevated abundances of moderately siderophile elements, FeO contents and oxygen fugacity[11,37] (Fig. 2, Extended Data Fig. 3). Many plume-related materials contain these geochemical signals, including elevated Ni contents and elevated oxygen fugacity[68–70] but (as emphasized in the main text) plume mantle Xe is dominated (about 90% of total Xe) by a recycled component[2–4]. Given that the relative efficiency of Xe recycling is probably lower than other less fluid-mobile elements it is plausible that geochemical signatures of accretion in plume mantle will be overprinted by recycled materials.

Tungsten is fluid-mobile under conditions relevant to subduction[55], and this behaviour may be crucial to preserving W isotopic anomalies[25]. High P–T core formation generates mantle with elevated [W] (Extended Data Fig. 3), and this elevated [W] may also contribute to the long-term preservation of W anomalies. The fact that high P–T core formation generates mantle with elevated [W] also leads to the prediction that the magnitude of the W anomalies will be correlated with [W] in the mantle source (Extended Data Fig. 3).

According to the modelling presented here, the minimum core equilibration pressure that can generate the Xe and W isotopic signatures is about 55 GPa. Under these conditions, we predict mantle to form with [W] about $5\times$ that of primitive MORB mantle (Extended Data Fig. 3). Partitioning behaviour for W follows from ref. 18. Higher-pressure core formation would produce mantle with higher [W]. At the highest pressures considered here (80 GPa), mantle will form with [W] about $20\times$ compared to primitive MORB mantle. For Ni and Co, plume mantle will vary from about $2\times$ (55 GPa) to about $5\times$ primitive MORB values (80 GPa). Partitioning behaviour for Ni and Co follows from ref. 37. Primitive MORB source Ni and Co contents were calculated using the P–T–X identified as successful for matching bulk silicate Earth [W][63] and FeO (Supplementary Table 4), yielding bulk silicate Earth values for [Ni] and [Co] that are approximately $2\times$ lower than estimates[71]. Consequently, the relative trends, rather than the absolute values, of the MSE calculations are more useful in evaluating MSE behaviour and are presented here. We emphasize that these calculations are only applicable for plume mantle immediately following core formation. Components recycled into plume mantle will dilute any geochemical anomalies generated during the formation of plume mantle.

The effect of plume mantle on bulk silicate Earth [W] is not clear, owing to uncertainty regarding the volume of plume mantle and [W] in plume mantle. For example, plume mantle may be contained within modern large low-shear-velocity provinces, which comprise about 8% of the total mantle volume[72]. If this is true, modern plume mantle volume could range from around 8% of mantle volume to <1%. If plume mantle is 5% of mantle volume and contains around $20\times$ [W] of the primitive MORB source (the high endmember case), plume mantle would contribute half of the bulk mantle budget. However, if plume mantle is 1% of the total mantle volume and contains $5\times$ [W] of the primitive MORB source (the low endmember case), then plume mantle would contribute negligibly to the bulk mantle W budget. The most recent estimate[63] for BSE [W] is 13 ± 10 p.p.b., so a doubling of bulk mantle [W] is of similar order to current uncertainty estimates. Given that Ni and Co would be less enriched in plume mantle compared to W, the effect of plume mantle on Ni and Co bulk mantle budgets would be correspondingly smaller (Extended Data Fig. 3).

There are caveats to the expected correlation between the elevated [W] and W anomalies. Given that Xe is 90% overprinted by recycled materials in plume

mantle[2–4], it is expected that the W anomalies have been diluted since their generation. Creating larger initial W anomalies in the mantle (as would be required if modern W anomalies have been diluted) requires earlier core formation or lower [W] in plume mantle. Lower [W] in the plume mantle could be achieved if plume mantle formed under more reduced conditions than considered here or under C-rich conditions[16–18]. It is also possible that I was available at lower concentrations during plume mantle core formation. If true, this would allow plume mantle core formation to occur at pressures lower than 55 GPa, with correspondingly lower enrichments of W in plume mantle compared to MORB mantle. Thus, the approximately 5× increase of [W] in the plume mantle is only a minimum value for the specific conditions considered here. Nonetheless, elevated [W] associated with W anomalies is a prediction of the present model.

The pressure and timing of core formation for MORB mantle are constrained here by identifying the *P*–timing space (*T* is fixed by the mantle liquidus of ref. 22) within a single-stage model that results in values for $^{182}W/^{184}W$, [W], and [FeO] within the permissible range for the bulk silicate Earth (Supplementary Table 4). To calculate the $f^{Hf/W}$ value associated with the evolution of $^{182}W/^{184}W$ in the MORB mantle following core formation (equation (16)), we assume[63] $[Hf]_{BSE} = 280$ p.p.b. Successful single-stage models are found for $[W]_{BSE}$ ranging between 3.0 p.p.b. and 3.8 p.p.b., equating to a Hf/W_{BSE} range of 74–93. A lower Hf/W_{BSE} value of 18 is obtained by dividing best estimates of the $Hf/U_{chondrite}$ against W/U_{BSE} (12.0 ± 4.2 and 0.65 ± 0.45, 2σ)[63,73]. Calculating the corresponding uncertainty on the Hf/W_{BSE} ratio is complicated by the unknown covariance of $Hf/U_{chondrite}$ and W/U_{BSE} uncertainties. Taking the extreme upper limit of $Hf/U_{chondrite}$ and lower limit of W/U_{BSE} (negatively correlated uncertainties) yields an upper limit Hf/W_{BSE} ratio of 81. Thus, given the current parameterizations of W and FeO partitioning and $^{182}W/^{184}W$ constraints for CHUR and BSE[11,15,18], $[W]_{BSE}$ and $[FeO]_{BSE}$ can only be mutually satisfied in the single-stage core formation framework explored here at the upper limit of the potential Hf/W_{BSE} range.

To calculate the value of $Hf/U_{chondrite}$ (12.0 ± 4.2) we average Hf/U measurements from ref. 73 for chondrites with $^{176}Hf/^{177}Hf$ ratios within error of the accepted value for chondrites of low metamorphic grade (0.282785 ± 0.000036, 2σ). We screen for accepted $^{176}Hf/^{177}Hf$ ratios in our averaging because elemental fractionations of Hf from U and Lu can occur during metamorphism on chondrite parent bodies[73], obscuring the bulk parent body U/Hf ratio. Fractionation of Hf from U and Lu is evidenced by a negative correlation between $^{176}Hf/^{177}Hf$ and Hf/U ratios within chondritic materials (not shown).

We emphasize that a single-stage core formation model is an endmember calculation. Expanding the present model to include multiple stages, non-liquidus temperatures, sulphur, carbon or changing oxygen content would enable greater overlap between the successful model Hf/W_{BSE} ratios and the geochemically constrained range of Hf/W_{BSE}. The offset between successful model Hf/W_{BSE} values and the best estimate of Hf/W_{BSE} does not change the essential result of the modelling, which is that mantle that experiences core formation, on average, under high pressures and early compared to the MORB mantle can evolve the range of W and Xe anomalies documented in plume rocks and will be predisposed to long-term preservation.

Data availability. The data supporting the findings of this study are available within the paper and its Supplementary Information.

31. Thibault, Y. & Walter, M. J. The influence of pressure and temperature on the metal-silicate partition coefficients of nickel and cobalt in a model C1 chondrite and implications for metal segregation in a deep magma ocean. *Geochim. Cosmochim. Acta* **59,** 991–1002 (1995).
32. Du, Z. *et al.* Using stepped anvils to make even insulation layers in laser-heated diamond-anvil cell samples. *Rev. Sci. Instrum.* **86,** 095103 (2015).
33. Akahama, Y. & Kawamura, H. Pressure calibration of diamond anvil Raman gauge to 310 GPa. *J. Appl. Phys.* **100,** 043516 (2006).
34. Prescher, C. & Prakapenka, V. B. DIOPTAS: a program for reduction of two-dimensional X-ray diffraction data and data exploration. *High Press. Res.* **35,** 223–230 (2015).
35. Andrault, D. *et al.* Thermal pressure in the laser-heated diamond-anvil cell: an X-ray diffraction study. *Eur. J. Mineral.* **10,** 931–940 (1998).
36. Tange, Y., Nishihara, Y. & Tsuchiya, T. Unified analyses for *P–V–T* equation of state of MgO: a solution for pressure-scale problems in high *P–T* experiments. *J. Geophys. Res. Solid Earth* **114** (B3), (2009).
37. Fischer, R. A. *et al.* High pressure metal–silicate partitioning of Ni, Co, V, Cr, Si, and O. *Geochim. Cosmochim. Acta* **167,** 177–194 (2015).
38. Du, Z. & Lee, K. K. High-pressure melting of MgO from (Mg, Fe) O solid solutions. *Geophys. Res. Lett.* **41,** 8061–8066 (2014).
39. Hirschmann, M. M., Baker, M. B. & Stolper, E. M. The effect of alkalis on the silica content of mantle-derived melts. *Geochim. Cosmochim. Acta* **62,** 883–902 (1998).
40. Liu, J., Li, J. & Ikuta, D. Elastic softening in Fe_7C_3 with implications for Earth's deep carbon reservoirs. *J. Geophys. Res. Solid Earth* **121,** 1514–1524 (2016).
41. Basu, S., Lahiri, A. K. & Seetharaman, S. Activity of iron oxide in steelmaking slag. *Metall. Mater. Trans. B* **39,** 447–456 (2008).
42. Japan Society for the Promotion of Science (JSPS) and the Nineteenth Committee on Steelmaking. *JSPS Steelmaking Data Sourcebook* 273–297 (Gordon and Breach Science Publishers, 1988).
43. Wade, J. & Wood, B. Core formation and the oxidation state of the Earth. *Earth Planet. Sci. Lett.* **236,** 78–95 (2005).
44. Ohnishi, S., Kuwayama, Y. & Inoue, T. Melting relations in the MgO–$MgSiO_3$ system up to 70 GPa. *Phys. Chem. Mineral.* **44,** 1–9 (2017).
45. Kilburn, M. & Wood, B. Metal–silicate partitioning and the incompatibility of S and Si during core formation. *Earth Planet. Sci. Lett.* **152,** 139–148 (1997).
46. Rubie, D. C., Gessmann, C. K. & Frost, D. J. Partitioning of oxygen during core formation on the Earth and Mars. *Nature* **429,** 58–61 (2004).
47. Dalou, C., Hirschmann, M. M., von der Handt, A., Mosenfelder, J. & Armstrong, L. S. Nitrogen and carbon fractionation during core–mantle differentiation at shallow depth. *Earth Planet. Sci. Lett.* **458,** 141–151 (2017).
48. Li, Y., Dasgupta, R., Tsuno, K., Monteleone, B. & Shimizu, N. Carbon and sulfur budget of the silicate Earth explained by accretion of differentiated planetary embryos. *Nat. Geosci.* **9,** 781–785 (2016).
49. Pepin, R. O. & Porcelli, D. Xenon isotope systematics, giant impacts, and mantle degassing on the early Earth. *Earth Planet. Sci. Lett.* **250,** 470–485 (2006).
50. Kendrick, M. *et al.* Seawater cycled throughout Earth's mantle in partially serpentinized lithosphere. *Nat. Geosci.* **10,** 222–228 (2017).
51. Touboul, M., Puchtel, I. S. & Walker, R. J. Tungsten isotopic evidence for disproportional late accretion to the Earth and Moon. *Nature* **520,** 530–533 (2015).
52. Kruijer, T. S., Kleine, T., Fischer-Gödde, M. & Sprung, P. Lunar tungsten isotopic evidence for the late veneer. *Nature* **520,** 534–537 (2015).
53. Heber, V. S., Brooker, R. A., Kelley, S. P. & Wood, B. J. Crystal-melt partitioning of noble gases (helium, neon, argon, krypton, and xenon) for olivine and clinopyroxene. *Geochim. Cosmochim. Acta* **71,** 1041–1061 (2007).
54. Smye, A. J. *et al.* Noble gases recycled into the mantle through cold subduction zones. *Earth Planet. Sci. Lett.* **471,** 65–73 (2017).
55. Bali, E., Keppler, H. & Audetat, A. The mobility of W and Mo in subduction zone fluids and the Mo–W–Th–U systematics of island arc magmas. *Earth Planet. Sci. Lett.* **351/352,** 195–207 (2012).
56. Matsuda, J. & Nagao, K. Noble gas abundances in a deep sea sediment core from eastern equatorial Pacific. *Geochem. J.* **20,** 71–80 (1986).
57. Staudacher, T. & Allegre, C. J. Recycling of oceanic crust and sediments—the noble gas subduction barrier. *Earth Planet. Sci. Lett.* **89,** 173–183 (1988).
58. Chavrit, D. *et al.* The contribution of hydrothermally altered ocean crust to the mantle halogen and noble gas cycles. *Geochim. Cosmochim. Acta* **183,** 106–124 (2016).
59. Kendrick, M. A., Honda, M. & Vanko, D. A. Halogens and noble gases in Mathematician Ridge meta-gabbros, NE Pacific: implications for oceanic hydrothermal root zones and global volatile cycles. *Contrib. Mineral. Petrol.* **170,** 43 (2015).
60. Kendrick, M. A., Scambelluri, M., Honda, M. & Phillips, D. High abundances of noble gas and chlorine delivered to the mantle by serpentinite subduction. *Nat. Geosci.* **4,** 807–812 (2011).
61. König, S., Münker, C., Schuth, S. & Garbe-Schönberg, D. Mobility of tungsten in subduction zones. *Earth Planet. Sci. Lett.* **274,** 82–92 (2008).
62. Harper, C. L. & Jacobsen, S. B. Evidence for ^{182}Hf in the early Solar System and constraints on the timescale of terrestrial accretion and core formation. *Geochim. Cosmochim. Acta* **60,** 1131–1153 (1996).
63. Arevalo, R. & McDonough, W. F. Tungsten geochemistry and implications for understanding the Earth's interior. *Earth Planet. Sci. Lett.* **272,** 656–665 (2008).
64. O'Brien, D. P., Walsh, K. J., Morbidelli, A., Raymond, S. N. & Mandell, A. M. Water delivery and giant impacts in the 'Grand Tack' scenario. *Icarus* **239,** 74–84 (2014).
65. Matsuda, J. *et al.* Noble gas partitioning between metal and silicate under high pressures. *Science* **259,** 788–790 (1993).
66. Sudo, M., Ohtaka, O. & Matsuda, J. Noble gas partitioning between metal and silicate under high pressures: the case of iron and peridotite. In *Noble Gas Geochemistry and Cosmochemistry* (ed. Matsuda, J.) 217–227 (Terra Scientific, 1994).
67. Bouhifd, M., Jephcoat, A. P., Heber, V. S. & Kelley, S. P. Helium in Earth's early core. *Nat. Geosci.* **6,** 982–986 (2013).
68. Chidester, B. A., Rahman, Z., Righter, K. & Campbell, A. J. Metal–silicate partitioning of U: implications for the heat budget of the core and evidence for reduced U in the mantle. *Geochim. Cosmochim. Acta* **199,** 1–12 (2017).
69. Herzberg, C. *et al.* Nickel and helium evidence for melt above the core–mantle boundary. *Nature* **493,** 393–397 (2013).
70. Moussallam, Y. *et al.* The impact of degassing on the oxidation state of basaltic magmas: a case study of Kīlauea volcano. *Earth Planet. Sci. Lett.* **450,** 317–325 (2016).
71. McDonough, W. F. & Sun, S. S. The composition of the Earth. *Chem. Geol.* **120,** 223–253 (1995).
72. Cottaar, S. & Lekic, V. Morphology of seismically slow lower-mantle structures. *Geophys. J. Int.* **207,** 1122–1136 (2016).
73. Dauphas, N. & Pourmand, A. Hf–W–Th evidence for rapid growth of Mars and its status as a planetary embryo. *Nature* **473,** 489–492 (2011).

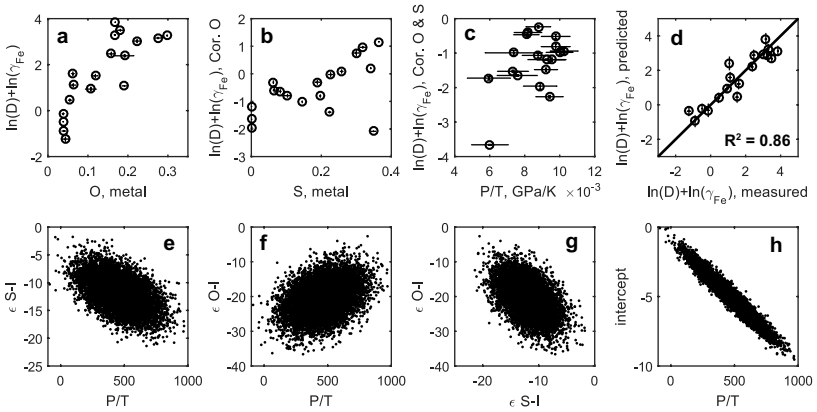

Extended Data Figure 1 | Parameterization of I partitioning between liquid Fe alloy and silicate liquid. a, Partitioning of I plotted against the O content (atomic) of metal phases. Oxygen content of the metal is the first parameter identified in the stepwise fitting approach. Higher O contents of metal are associated with greater partitioning of I into metal over silicate. **b**, Partitioning of I corrected to O-free metal plotted against S content of metal. The S content of the metal is the second parameter identified in the stepwise fitting approach. **c**, Partitioning of I corrected to O- and S-free metal plotted against P/T. The P/T term is the third parameter identified in the stepwise fitting approach. **d**, A comparison of observed and predicted I partitioning. I partitioning is predicted using equation (1) ($R^2 = 0.86$). **e**–**h**, Covariance plots of parameterization. 'Intercept' refers to the constant term in equation (1).

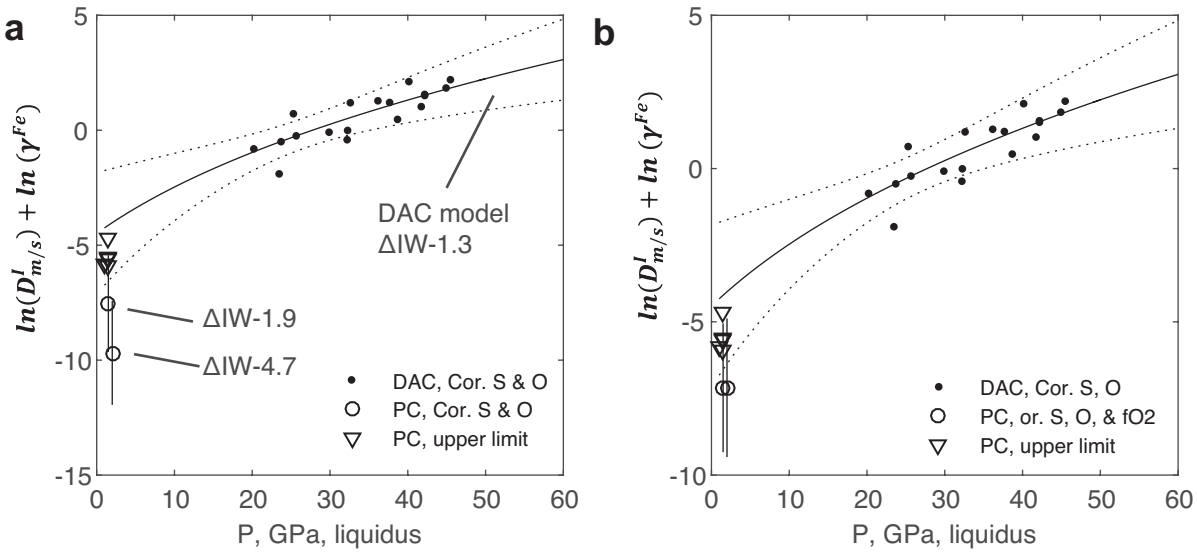

Extended Data Figure 2 | Piston cylinder data comparison with DAC regression. a, A comparison of I partition coefficients determined in piston cylinder (PC) experiments and the I partition coefficient predicted from equation (1). Piston cylinder data are corrected to remove the effect of S and to the O contents of metal predicted along the mantle liquidus of ref. 22, allowing a direct comparison to the DAC data model. Upper-limit partition coefficients are consistent with the lower end of the uncertainty envelope. The difference in measured I partitioning coefficients in the piston cylinder series suggests that I partitioning is redox sensitive. **b**, Measured partition coefficients in piston cylinder series are corrected to ΔIW−1.3 and offset in pressure for clarity. Error bars and the uncertainty envelope are 2σ.

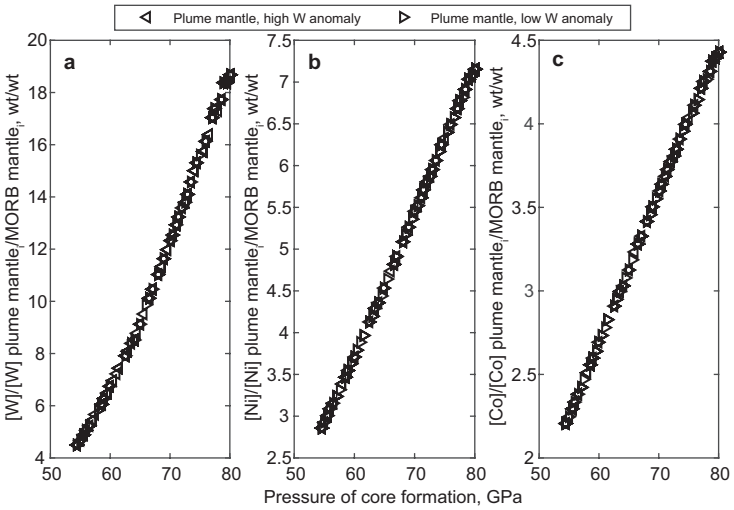

Extended Data Figure 3 | Calculated concentration of MSEs in plume mantle as a function of the pressure of core–mantle equilibrium. W (**a**), Ni (**b**), and Co (**c**) concentrations in plume mantle all increase with increasing core–mantle equilibrium pressure. Results are normalized to the calculated concentration of MORB MSEs. MORB MSE concentrations are calculated using the average *P*–*T*–*X* conditions that satisfy BSE [W] and [FeO] (Supplementary Table 4). Temperatures are assumed to follow the mantle liquidus of ref. 22. FeO abundances are calculated following ref. 11. W partitioning is from ref. 18. Ni and Co partitioning are from ref. 37. Plume mantle data points are plotted only for *P*–*T*–*X* conditions that satisfy W and Xe isotopic constraints (see Methods subsection 'Calculation of W and Xe isotopic anomalies resulting from discrete stages of core formation').

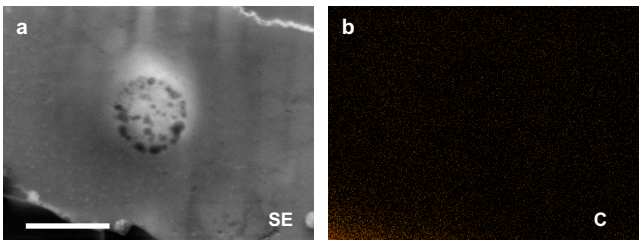

Extended Data Figure 4 | Imaging of silicate following analysis with low electron microprobe total. a, Secondary electron (SE) image of the DAC_I_EXP5 spot 4 silicate shows evidence of vesiculation in the area that was analysed. **b**, C map showing no obvious concentration of C local to vesiculation. The dark material in the lower left corner of **a** is diamond. Scale bar is 1 μm.

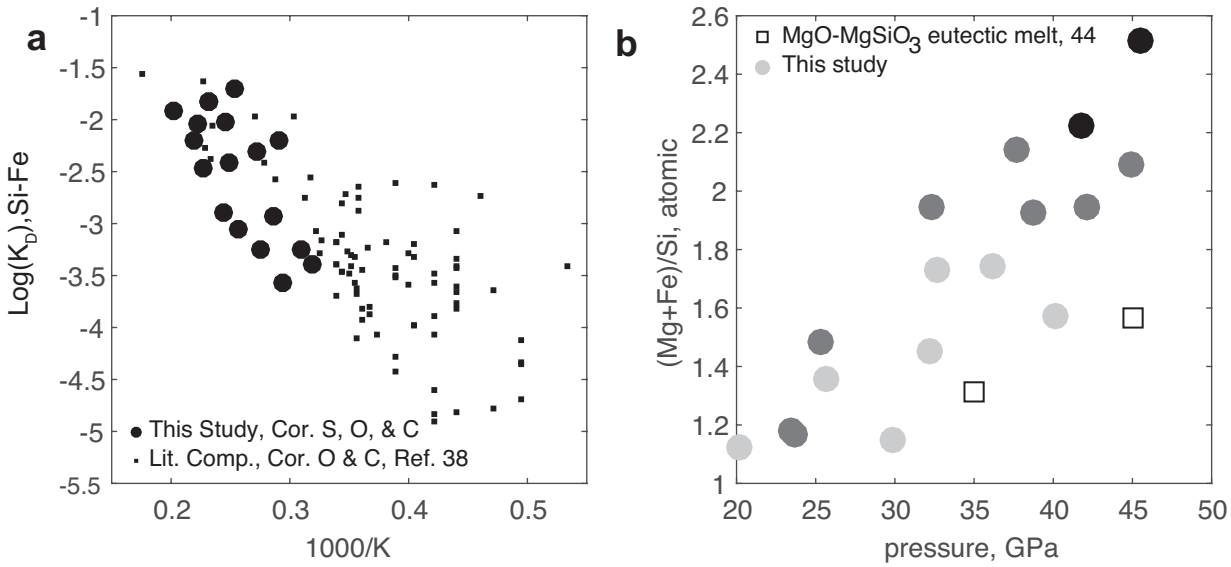

Extended Data Figure 5 | Demonstrations of DAC experiment equilibrium. a, Si–Fe exchange coefficient plotted against inverse temperature. Data from this study (circles) are corrected for S–O–C interactions with silicon. Squares are from the compilation of ref. 37 corrected from O–C interactions with silicon. **b**, (Mg+Fe)/Si ratios of the silicate phase from this study (circles) and ref. 44 (squares) plotted against pressure. Symbols are grouped for Mg#, with darker symbols corresponding to lower Mg#. The offset of lower Mg# silicates within a pressure range to higher (Mg+Fe)/Si ratios and the similar pressure slopes within Mg# groupings support the accuracy of our pressure calculations.

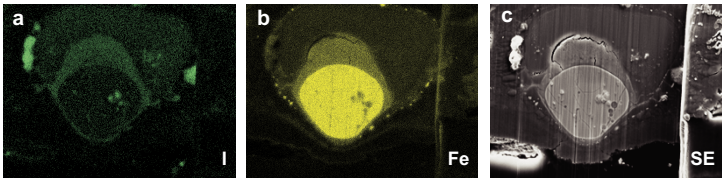

Extended Data Figure 6 | Secondary electron image and EDS maps of experiment DAC_I_EXP9 spot 4 showing I mobility. The sequence of images shows the nature and distribution of I-rich materials that are mobilized to the surface of heating spots after storage in desiccators. **a**, Map of I distribution. I-rich materials are concentrated along the left and right edges of the heating spot, within isolated regions of the metal and silicate phases, and surrounding the Fe alloy phase. **b**, Map of Fe distribution. The metallic phase is mantled by Fe-rich and I-rich material. This material is also rich in C and O (not shown). The I-rich material that is present along the edges of the heating spot is also enriched in Fe, C and O. **c**, Secondary electron image. I-rich materials are positive relief features. Images are 20 μm wide.

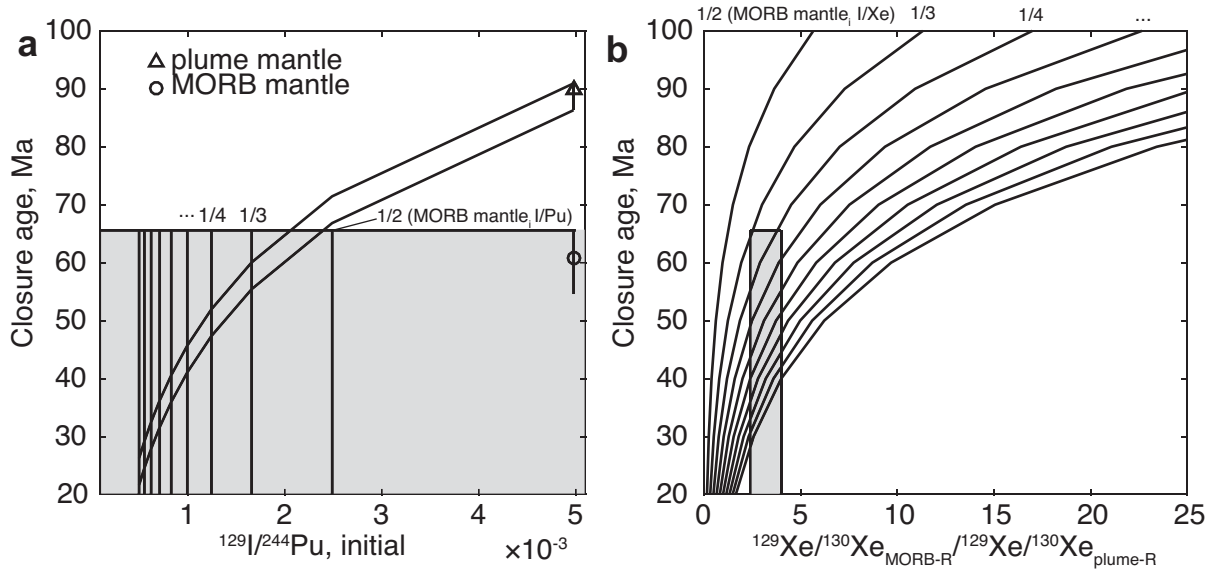

Extended Data Figure 7 | Parent–daughter ratio variations required to account for Xe isotopic variability between plume and MORB mantle. **a**, Closure ages plotted against initial ^{129}I/^{244}Pu ratios. Closure ages are calculated using ^{129}Xe*/^{136}Xe$_{Pu}$ ratios from ref. 8 and equation (12). The MORB mantle ^{129}I/^{244}Pu ratio is fixed and derived from estimates for the bulk silicate Earth from refs 49 and 50. The grey shading delineates I–Pu–Xe closure ages that are equal to or less than that determined for MORB mantle. Vertical lines in the grey shaded area are fractional depletions of the I/Pu in plume mantle relative to MORB mantle, ordered sequentially. The ratios denote the fractional depletion of the I/Pu ratio for plume mantle relative to initial MORB mantle. An approximately 3× lower I/Pu ratio for plume mantle results in equal closure ages for MORB and plume mantle. **b**, Closure ages plotted against the ratio of radiogenic components for ^{129}Xe/^{130}Xe within MORB and plume mantle. The upper edge of the grey shaded area delineates the upper limit of MORB mantle I–Pu–Xe closure. Left and right edges delineate the uncertainty on the ratio of radiogenic components observed in MORB and plume mantle. Curves are calculations for the ratio of radiogenic components of ^{129}Xe/^{130}Xe (denoted '–R', see equation (13)), assuming different fractional depletions of the I/Xe ratio in plume mantle relative to initial MORB mantle (see fractions plotted along edge of graph). These calculations assume a MORB mantle closure age of 61 million years (Ma).